metals

MDPI

Article

Effect of Welding Heat Input on Microstructure and Impact Toughness in the Simulated CGHAZ of Low Carbon Mo-V-Ti-N-B Steel

Mingliang Qiao [1,2], Huibing Fan [1,2], Genhao Shi [1,2], Leping Wang [1,2], Qiuming Wang [1,2], Qingfeng Wang [1,2,*] and Riping Liu [1]

[1] State Key Laboratory of Metastable Materials Science and Technology, Yanshan University, Qinhuangdao 066004, China; 13191816617@163.com (M.Q.); 15033576807@163.com (H.F.); shigenhao@foxmail.com (G.S.); wlp97@stumail.ysu.edu.cn (L.W.); wqm931028@stumail.ysu.edu.cn (Q.W.); tjutws@163.com (R.L.)

[2] National Engineering Research Center for Equipment and Technology of Cold Strip Rolling, Yanshan University, Qinhuangdao 066004, China

* Correspondence: wqf67@ysu.edu.cn

Abstract: Welding thermal cycles with heat inputs ranging from 25 to 75 kJ/cm were performed on a Gleeble 3500. The impact energy improved significantly (from 10 to 112 J), whereas the simulated coarse-grain heat-affected zone (CGHAZ) microstructure changed from lath bainite ferrite (LBF) and granular bainite ferrite (GBF) + martensite/austenite (M/A) to acicular ferrite (AF) + polygonal ferrite (PF) + M/A as the heat input increased. Simultaneously, the mean coarse precipitate sizes and the degree of V(C,N) enrichment on the precipitate surface increased, which provided favorable conditions for intragranular ferrite nucleation. The Ar_3 of CGHAZ increased from 593 °C to 793 °C with increasing heat inputs; the longer high-temperature residence time inhibited the bainite transformation and promoted the ferrite transformation. As a result, acicular ferrite increased and bainite decreased in the CGHAZ. The CGHAZ microstructure was refined for the acicular ferrite segmentation of the prior austenite, and the microstructure mean equivalent diameter (MED) in the CGHAZ decreased from 7.6 μm to 4.2 μm; the densities of grain boundaries higher than 15° increased from 20.3% to 45.5% and significantly increased the impact toughness. The correlation of heat input, microstructure, and impact toughness was investigated in detail. These results may provide new ideas for the development of high welding heat input multiphase steels.

Keywords: low-carbon Mo-V-Ti-N-B steel; heat input; microstructure; intragranular ferrite; impact toughness

check for updates

Citation: Qiao, M.; Fan, H.; Shi, G.; Wang, L.; Wang, Q.; Wang, Q.; Liu, R. Effect of Welding Heat Input on Microstructure and Impact Toughness in the Simulated CGHAZ of Low Carbon Mo-V-Ti-N-B Steel. *Metals* **2021**, *11*, 1997. https://doi.org/10.3390/met11121997

Academic Editor: José María Rodríguez-Ibabe

Received: 7 October 2021
Accepted: 7 December 2021
Published: 10 December 2021

Publisher's Note: MDPI stays neutral with regard to jurisdictional claims in published maps and institutional affiliations.

Copyright: © 2021 by the authors. Licensee MDPI, Basel, Switzerland. This article is an open access article distributed under the terms and conditions of the Creative Commons Attribution (CC BY) license (https://creativecommons.org/licenses/by/4.0/).

1. Introduction

Due to its good toughness and high strength, high-strength micro-alloy steel has been utilized broadly to build large ships, high-rise buildings, and heavy-duty steel bridges [1–4]. However, high-strength steel comes with many problems and challenges during welding. For example, high-strength steel suffers from cold cracking when welded in a wet environment [5,6]. In addition, a CGHAZ forms when high-strength, low-alloy steel undergoes rapid heating and high peak temperature welding. Coarse grains formed in the CGHAZ at a peak temperature of 1320 °C or higher [7–11]. In CGHAZ, austenite grains coarsened and brittle structures, such as a M/A constituents, coarse-grain boundary ferrite, and granular bainite, formed in the grains and significantly deteriorated the toughness [11–14]. This reduction is particularly serious in high heat inputs. However, considering welding efficiency and economic cost, electroslag welding and gas-electric vertical welding using a high heat input have been utilized extensively [15,16]. A high heat input caused coarse CGHAZ microstructures and the impact toughness was seriously affected because of the slow cooling speed and long high-temperature residence time.

The microstructures and properties of CGHAZ relate closely to the thermal welding cycle. Welding heat inputs generally correlate negatively with the CGHAZ mechanical properties. Higher heat inputs result in coarser microstructures and lower impact properties [17]. Hence, studying the microstructure and impact toughness of CGHAZ under different heat inputs is necessary. Lan et al. [18,19] reported the impact toughness of CGHAZ in low-carbon bainitic steel deteriorated with an increased heat input, which was primarily associated with the large M/A constituent and coarse bainite. The large-sized, hard M/A constituent led to local embrittlement and crack initiation [20–22]. A refined microstructure increases the high-angle boundary density, which is very useful for preventing crack propagation and enhancing crack propagation energy [23–25]. Acicular ferrite (AF) partitions the austenite grain into several regions and refines the final microstructure, which effectively improves the impact toughness of CGHAZ [25–27]. Recently, the addition of nitrogen into the V-Ti micro-alloyed steel contributed to the intragranular ferrite transformation of CGHAZ. Shi et al. [28,29] conducted a comparison of a simulated CGHAZ microstructure and mechanical properties between V-Ti and V-N-Ti steels. The N-enhanced steel contained numerous (Ti, V) (C, N) particles on which AF nucleates, which led to a lower ductile–brittle transition temperature for the simulated CGHAZ.

To refine the microstructure of CGHAZ under a high heat input, N micro-alloying provides a good design idea. Zhang et al. [30] revealed that the optimum impact toughness occurred using a high heat input; the increased formation of AF and HAGB remedied the detrimental effects caused by the coarsened PAG and M/A constituent. However, one noteworthy observation is that impact toughness increased along with increases in heat input in the low-carbon N-enhanced steel, though the details are unclear. Therefore, the evolution mechanism of the simulated CGHAZ microstructure and the impact toughness of low-carbon N-contained steel with different welding heat inputs both require further clarification.

In the present study, low-carbon Mo-V-Ti-N-B steel was modeled for a welding simulation, and the relationships between heat input, microstructure, and impact toughness of the CGHAZ were investigated in detail. This research plays a significant role in advancing the steel of high-heat-input welding in engineering applications.

2. Materials and Experimental

2.1. Materials

The chemical composition and mechanical properties of the low-carbon Mo-V-Ti-N-B steel that was melted in a 40 kg vacuum furnace (Central Iron & Steel Research Institute, Beijing, China) are listed in Tables 1 and 2, respectively.

Table 1. Chemical composition of low-C Mo-V-Ti-N-B steel (wt.%).

C	Si	Mn	P	S	Mo	V	Ti	N	B	Ceq
0.06	0.27	1.55	0.004	0.006	0.28	0.066	0.016	0.0110	0.0011	0.38

Table 2. The basic mechanical properties of low-C Mo-V-Ti-N-B steel.

Yield Stress	Tensile Stress	Elongation Rate	Impact Energy
523 MPa	645 MPa	20.26%	177 J

The equivalent carbon content (C_{eq}) of the experimental steel was calculated using Equation (1), which refers to (IIW); the result is shown in Table 1.

$$C_{eq} = C + \frac{Mn}{6} + \frac{Cr + Mo + V}{5} + \frac{Ni + Cu}{15} \quad (1)$$

2.2. Experimental

Cubical samples of 10.5 mm × 10.5 mm × 80 mm, obtained from hot-rolled plates in the rolling direction, were used for welding simulations on a Gleeble 3500 (Dynamic Systems Inc., New York, NY, USA) to study the microstructure and toughness changes in the CGHAZ with different heat inputs. Figure 1 shows the welding thermal cycle curves generated by the Rykalin 2D model equipped on the Gleeble 3500. The relationship between time and temperature can be calculated by using this model, as shown in Equation (2):

$$T_{(t)} = \frac{E}{\delta} \times \frac{1}{\sqrt{4\pi\lambda\rho ct}} exp\left[-\frac{r}{4(\lambda/\rho c)t}\right] \quad (2)$$

where $T_{(t)}$: real-time temperature; E: welding heat input (kJ/cm); δ: thickness of the sample (cm); λ: thermal conductivity of the sample (J/(cm × S × °C)); ρ: density of the sample (g/cm^3); t: the time (s); c: Specific heat capacity J/(g × °C); r: the distance from a point to the arc center line. The density of the tested steel in this paper is 7.8 g/cm^3, the specific heat capacity c is 0.586 J/(g × °C), the thermal conductivity λ is 0.36, the T_{max} is 1350 °C, and plate thickness is 18 mm.

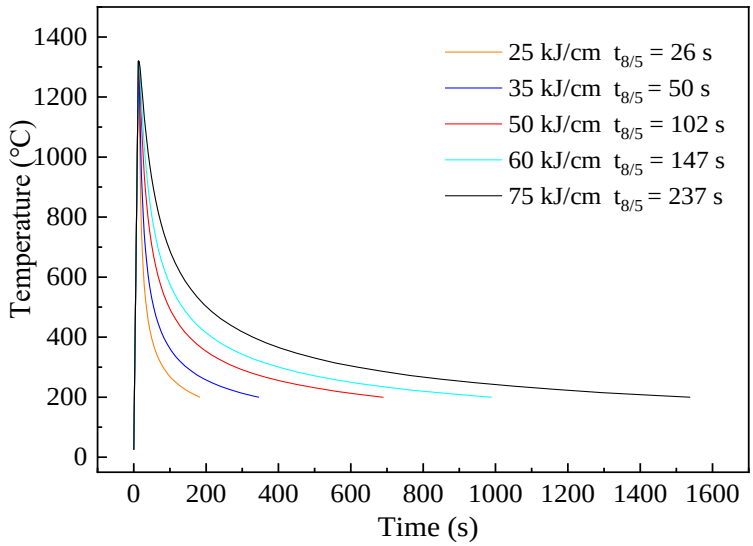


Figure 1. Thermal welding cycle curves of CGHAZ.

The samples were heated to 1350 °C at 100 °C/s and held for 1 s, and then the samples were cooled along the thermal cycles in Figure 1. The $t_{8/5}$ was selected as 26 s, 50 s, 102 s, 147 s, and 237 s to simulate different welding heating inputs, which equated to 25 kJ/cm, 35 kJ/cm, 50 kJ/cm, 60 kJ/cm, and 75 kJ/cm of in-service welding, respectively.

The simulated samples were processed into standard Charpy V-Notch (CVN) impact samples (Qinhuangdao Yanbang Machinery Processing CO., LTD, Qinhuangdao, China), and the absorbed impact energies of the samples were tested at −20 °C using a JB-300B impact tester (JINAN MARXTEST TECHNOLGGY CO., LTD, Jinan, CHN), according to GB/T 229-2007. The average impact energy was obtained by three impact experiments for each heat input. The surface morphologies of the impact samples were examined via scanning electron microscopy (SEM SU5000, HITACHI, Tokyo, Japan). The microstructural composition and crack propagation paths on the intersecting surface perpendicular to the fracture surface were examined.

Metallographic specimens taken from the zone adjacent to the thermocouple location were mechanically ground, polished, and etched with a 4% (by volume) Nital solution, as per GB/T 13298-2015, followed by an optical microscopy examination via the Olympus BX51M (Olympus, Aizu, Japan) and SEM. The chemical composition of the precipitated particles and the intracrystalline acicular ferrite nucleation were characterized by energy-

dispersive X-ray spectroscopy (EDS, Hitachi Limited, Tokyo, Japan). To characterize the M/A constituents in the simulated CGHAZ, metallographic samples were remade and etched using Lepera etchant (a 1:1 mixture of 1% sodium sulfite aqueous solution and 4% picric acid alcohol solution) for 45 s before being investigated by an Olympus BX51M optical microscope. Furthermore, the size and amount of the M/A constituents were calculated using Image-Pro Plus (Image-Pro ®Plus, Media Cybernetics, Bethesda, MD, USA). Samples for prior austenite and microstructure observations were etched with supersaturated picric acid and 4 vol.% Nital solutions. A standard line intercept determined the PAG sizes. Moreover, the precipitates and microstructures were also characterized using JEM-2010 high-resolution transmission electron microscopy (TEM, Japan Electronics optics Corporation, Tokyo Prefecture, Japan) and the compositions of the precipitates were detected by EDS. The samples for the TEM microstructure characterizations were cut from the metallographic samples and were ground until they were 30 μm thick, and then thinned by electropolishing in a 7% mixture of perchloric acid/glacial acetic acid with a voltage and current of 28 V and 50–65 mA, respectively. Finally, the thinned samples were made into 3-mm diameter disks for TEM observation. To observe the precipitates, the metallographic samples were polished; the carbon layer was cut into a square and deposited onto them. Finally, they were extracted with 4 vol.% Nital for TEM examination. In addition, the MED and the fraction of different misorientation tolerance angles (MTAs) of the simulated samples were determined by electron backscatter diffraction (EBSD, Hitachi Limited, Tokyo, Japan).

3. Results

3.1. Impact Results

The impact energies of the samples subjected to thermal welding are shown in Figure 2. The impact energy increased significantly (from 10 to 112 J) and the average percentage of the ductile fracture zones that appeared on the fracture surface increased from 0 to 47%, as the heat input rose from 25 to 75 kJ/cm.

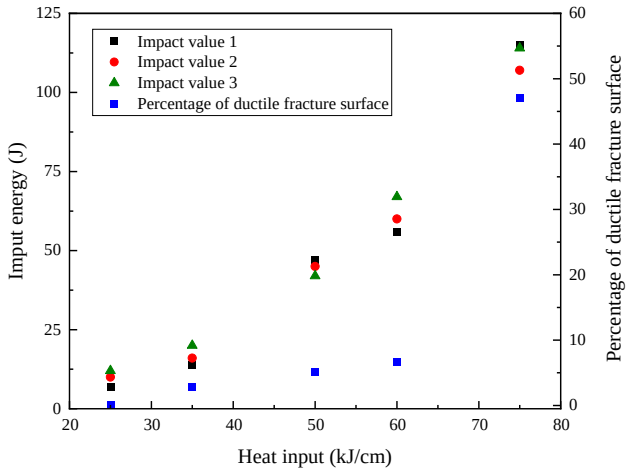


Figure 2. The impact energy and percentage of the ductile fracture surface of samples with different heat inputs.

3.2. Microstructure

The OM micrographs of the simulated samples for the different heat inputs are presented in Figure 3, and the corresponding microstructure features are summarized in Table 3. The microstructures of CGHAZ with a 25 kJ/cm thermal input were composed primarily of LBF and GBF. The LBF decreased and the GBF increased as the heat input increased from 25–50 kJ/cm. The CGHAZ microstructures were composed of GBF and AF (Figure 3c). By increasing the heat input to 60/75 kJ/cm, the PF and AF increased,

whereas the GBF decreased (Figure 3c–e). The 75 kJ/cm input sample contained a mixed microstructure of AF and PF (Figure 3e).

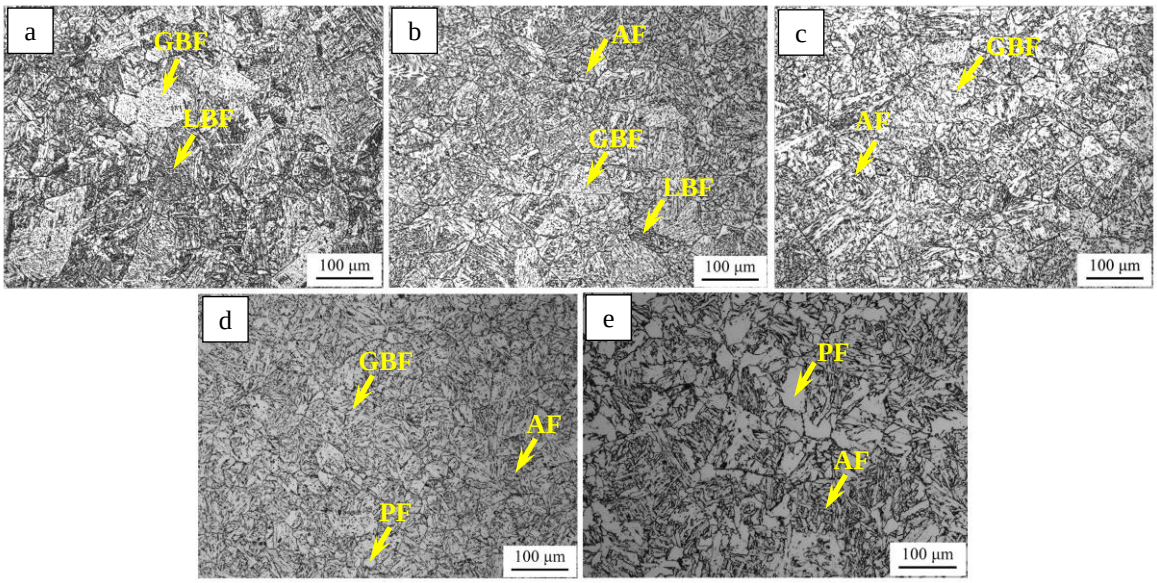


Figure 3. OM micrographs of the simulated samples' heat inputs of 25 kJ/cm (**a**), 35 kJ/cm (**b**), 50 kJ/cm (**c**), 60 kJ/cm (**d**), and 75 kJ/cm (**e**).

Table 3. Microstructure quantifications in the simulated samples.

Heat Input/kJ·cm^{-1}	Microstructure	$f_{M/A}$/%	$d_{M/A}$/μm	f_{MTA} > 15°	MED/μm
25	LBF + GBF + M/A	3.3	1.1	20.3	8.6
35	LBF + GBF + AF + M/A	3.6	1.4	24.7	7.9
50	GBF + AF + M/A	4.0	1.9	31.1	7.1
60	GBF + AF + PF + M/A	4.3	2.1	36.7	6.5
75	AF + PF + M/A	4.5	2.4	45.5	5.2

$f_{M/A}$—area fraction of M/A constituent, $d_{M/A}$—average diameter of M/A, MTA—misorientation tolerance angle, $f_{MTA>15°}$—fraction of boundaries at MTAs higher than 15°, MED—mean equivalent diameter of ferrite grain with boundaries at MTAs higher than 15°.

Figure 4 shows the evolution of the M/A constituents in CGHAZ with varied heat inputs. The M/A morphology changed from slender to blocky, and the levels of M/A increased along with the heat input (from 25–75 kJ/cm). Table 3 shows the quantified M/A changes.

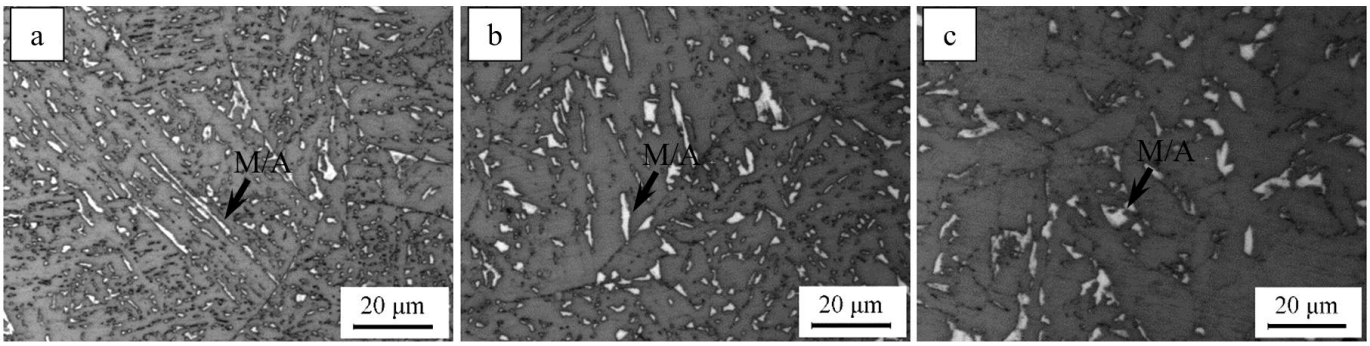


Figure 4. M/A constituent observations of the simulated CGHAZ with heat inputs of 25 kJ/cm (**a**), 50 kJ/cm (**b**), and 75 kJ/cm (**c**).

Figure 5 shows the TEM results of the ferrite matrix and the M/A constituents in CGHAZ with different heat inputs. The parallel LBF and GBF plates decreased while the AF plates and PF increased with increasing heat inputs. Considerable AF, PF, and M/A constituents were observed at a heat input of 75 kJ/cm (Figure 5c). Moreover, slender and blocky M/A constituents were scattered between the ferrite plates. The morphologies of the M/A constituents changed from slender to blocky with an increasing heat input. The bright field images (Figure 5d), the dark field images (Figure 5e), and the diffraction patterns (Figure 5f) show that the islands comprised martensite and austenite.

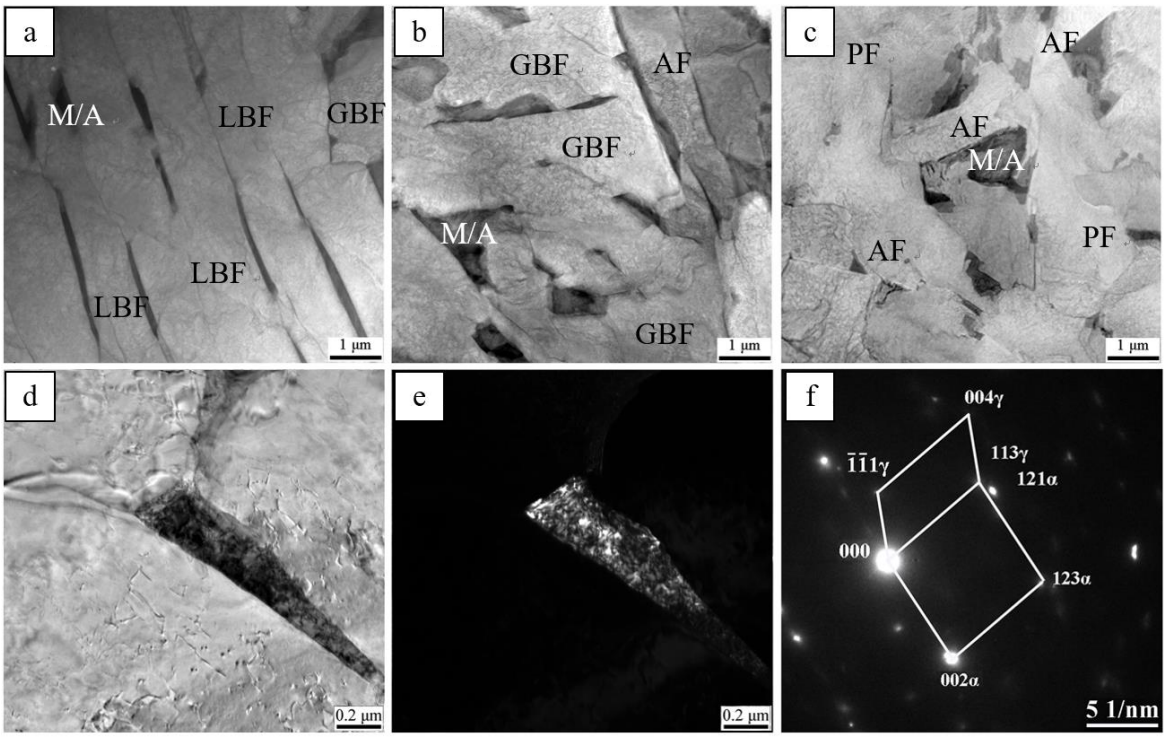


Figure 5. TEM micrographs of simulated CGHAZ at (**a**) 25 kJ/cm (**b**) 50 kJ/cm, and (**c**) 75 kJ/cm; the M/A constituent indicated by (**d**) bright field, (**e**) dark field, and (**f**) the selected area diffraction pattern.

The inverse pole figures (IPFs) of the simulated CGHAZ samples for different heat inputs are shown in Figure 6, and Figure 7 shows the distribution of the grain boundaries' misorientation tolerance angles (MTAs). The MTAs of 2–15° and >15° are represented by white and black lines, respectively. As Figure 6 shows, the internal MTAs of GBF and LBF were mainly low-angle grain boundaries, whereas the MTAs of AF and PF were high-angle grain boundaries. EBSD results revealed a MED decrease from 7.6 μm to 4.2 μm, and an increase in the f_{MTA} > 15° from 20.3% to 45.5%, as the heat input varied from 25 to 75 kJ/cm, respectively.

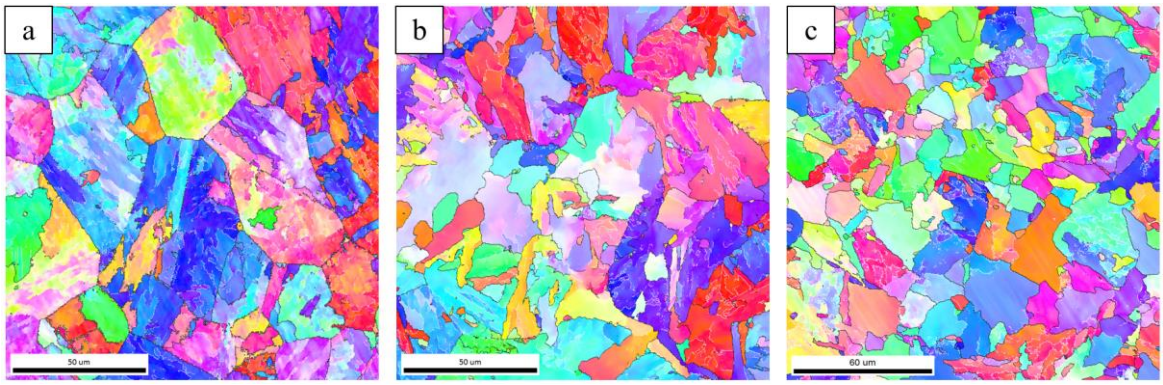


Figure 6. IPFs of the simulated samples with the heat inputs of 25 kJ/cm (**a**), 50 kJ/cm (**b**), and 75 kJ/cm (**c**).

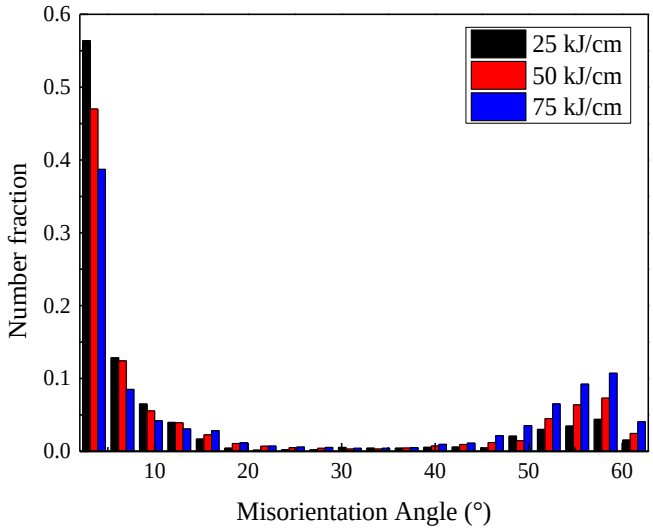


Figure 7. Distribution of MTA grain boundaries for simulated samples with different heat inputs.

Figure 8 displays micrographs of the sample precipitates quenched at 1320 °C and in the CGHAZs of the different heat input samples. Precipitates were divided into coarse and fine precipitates based on their size. Coarse precipitates, from 0.1–0.3 μm in diameter, were classified into Ti(C,N) or (Ti,V)(C,N) according to their chemical compositions as analyzed by EDS. Fine precipitates, from 10–80 nm, were mainly (V,Ti)(C,N) and V(C,N). Figure 9a shows the statistical results of the precipitates in the quenched sample and the simulated CGHAZ samples with different heat inputs. An almost-equal density of coarse precipitates, ranging from 0.47–0.51 per square micron, appeared in each sample, whereas the density of fine particles increased sharply with increasing inputs (from 25 to 75 kJ/cm). In addition, the average size of the coarse precipitates increased significantly, as shown in Figure 9b.

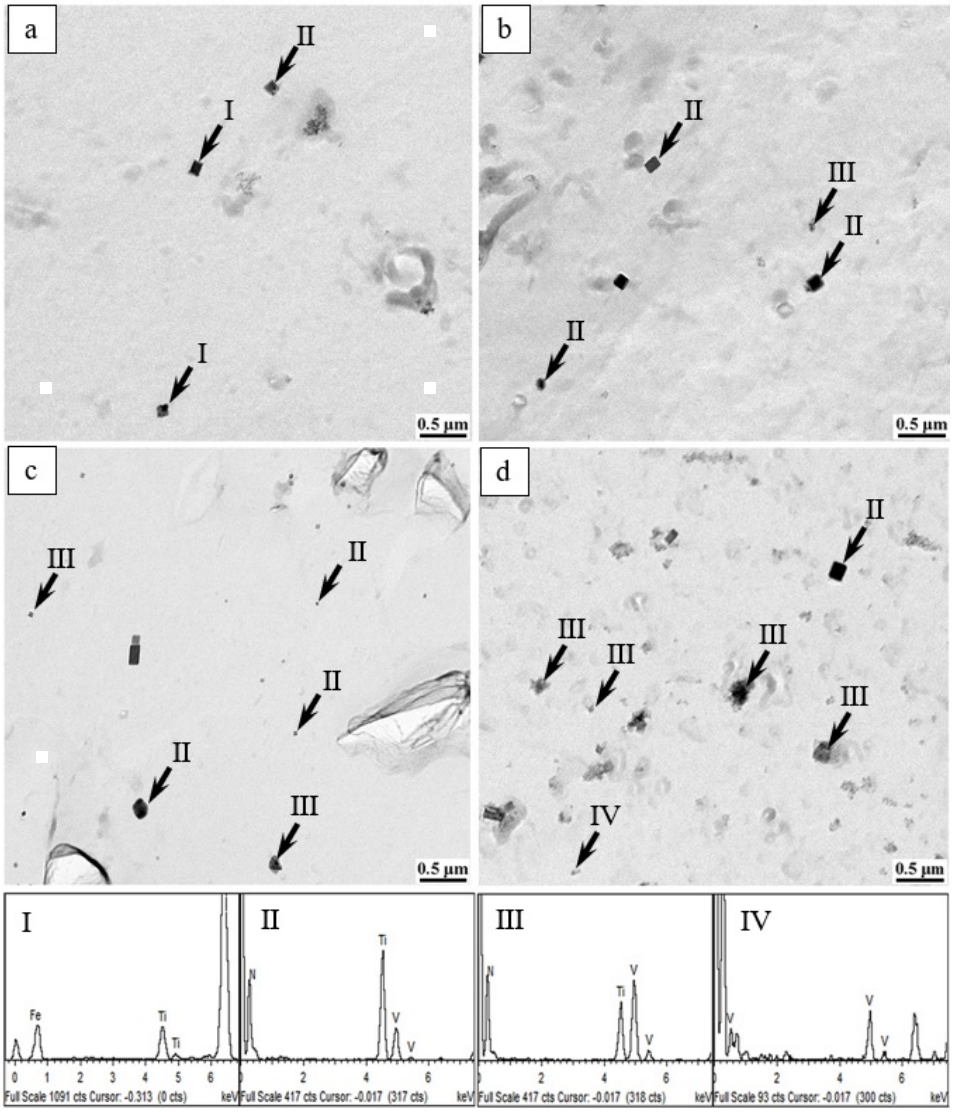


Figure 8. TEM observations of coarse and fine precipitates in quenched samples (**a**), simulated CGHAZ samples with input heats of 25 kJ/cm (**b**), 50 kJ/cm (**c**), 75 kJ/cm (**d**), and their chemical compositions analyzed by EDS.

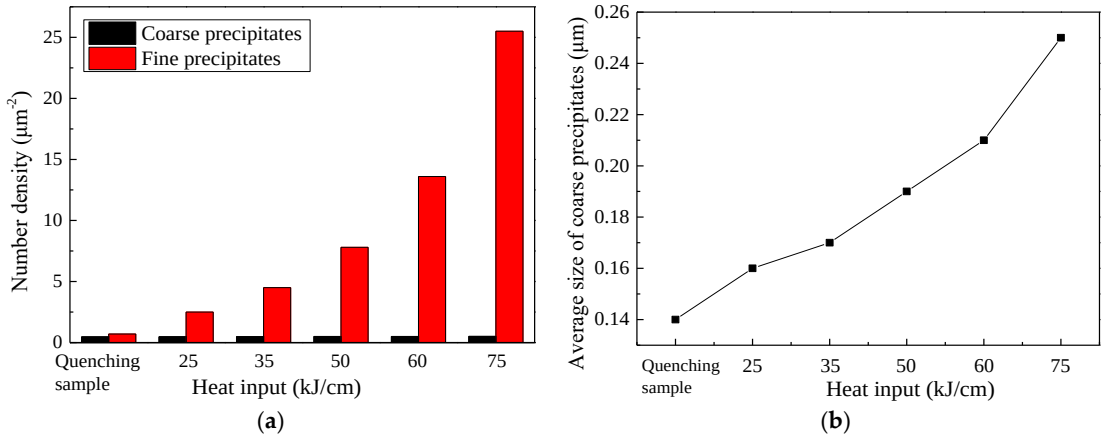


Figure 9. The precipitate density (**a**) and the average size of coarse precipitates (**b**) in the quenched samples and samples with different heat inputs.

3.3. Fracture Behaviors

The fracture surface micrographs of the simulated CGHAZ samples with different heat inputs are presented in Figure 10a–c. As shown in Figure 10a-I and Figure 10a-II for 25 kJ/cm, the fracture surface had no ductile fracture zone and the brittle zone comprised numerous large cleavage facets. Moreover, the micrographs of the ductile zones for 50 and 75 kJ/cm are shown in Figure 10b-III and Figure 10c-V, and illustrate the morphology of the dimples. Plentiful parabola-shaped dimples connected by micro-dimples appeared in the ductile zone and the depth of the dimples deepened with increasing heat inputs. Meanwhile, Figure 10b-IV and Figure 10c-VI exhibit the micrographs of the brittle zones for 50 and 75 kJ/cm and show the typical fracture surface of the cleavage facet appearance. Some cleavage cracking facets, with long river pattern trips connected to tear ridges and the cleavage facet sizes, decreased with increasing heat inputs. Tear ridges, together with dimples, arose in the brittle zone for 75 kJ/cm.

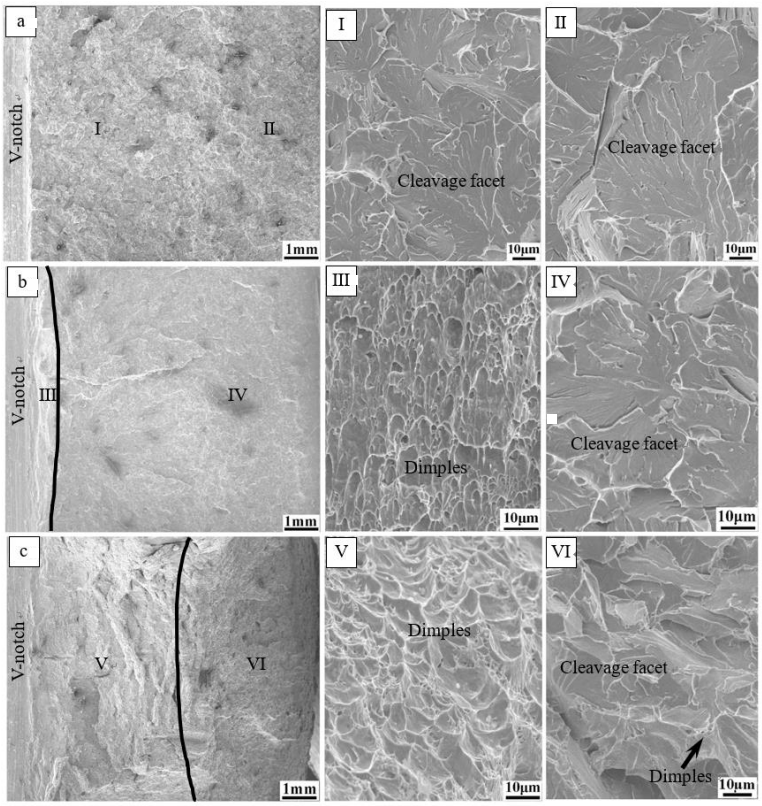


Figure 10. Fracture surfaces of the impact samples with a heat input of 25 kJ/cm (**a**), 50 kJ/cm (**b**), and 75 kJ/cm (**c**) and local features of the ductile zone (**I**/**III**/**V**) and the brittle zone (**II**/**IV**/**VI**).

4. Discussion

4.1. Effects of Increasing Heat Input on Simulated CGHAZ Microstructures

As shown in Figure 8, precipitates of the quenched samples were primarily Ti(C,N) with dimensions between 0.1–0.2 μm, whereas (Ti,V)(C,N), (V,Ti)(C,N), and V(C,N) appeared in samples with different heat inputs. Furthermore, the amount of (V,Ti)(C,N) and V(C,N) increased, and the dimensions of the coarse precipitates increased with increasing heat inputs.

Thermodynamic computations were conducted and are shown in Figure 11, indicating that Ti(C,N) and V(C,N) began precipitation at 1503 °C and 1012 °C, respectively. Most of the V-rich precipitates dissolved, while only part of the Ti-rich precipitates dissolved during heating, which resulted in coarse undissolved Ti(C,N) in the sample quenched at 1320 °C. The formation of complex precipitates, namely, (Ti,V)(C,N) and (V,Ti)(C,N), relates to precipitation behavior during cooling. Because of differences in precipitation

temperature, the precipitation of Ti-rich precipitates preferentially occurred during cooling, while V-rich precipitates formed later. Fine Ti-rich precipitates and coarse undissolved Ti(C,N) acted as nucleation sites for V(C,N), so the complex precipitates comprised a Ti-rich core and a V-rich cap.

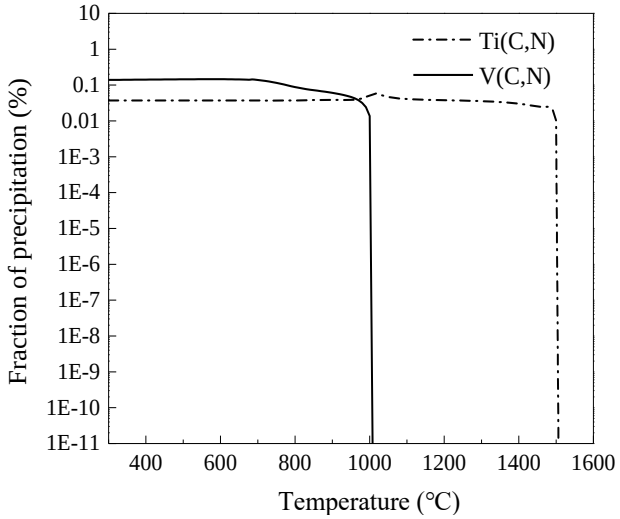


Figure 11. Fraction of V(C,N) and Ti(C,N) as a function of temperature for the experimental steel.

From the quenched sample to the increasing heat input samples, the cooling rate decreased and extended the high-temperature residence time, which contributed to the diffusion of Ti and V. Moreover, the precipitation of V was more intense than Ti during cooling, due to the more sufficient solution of V during heating. Therefore, the primary precipitate changed from Ti-rich to V-rich, and the dimension of the coarse precipitates increased with the increasing heat input.

The relationship between precipitate and intragranular ferrite nucleation was observed and is now discussed in detail. Figure 12 shows that the 0.3-μm precipitates promoted the nucleation of intragranular ferrite in the 75 kJ/cm sample. This nucleation was primarily due to two factors. On one hand, the precipitation of V(C,N) increased and the degree of V(C,N) enrichment on the precipitate surface increased with increasing heat inputs, which provided the basic thermal conditions required for intragranular ferrite nucleation. On the other hand, the average size of the coarse precipitates increased significantly, from 0.14 to 0.25 μm, with increasing heat inputs (Figure 9b), which reached the critical size for nucleation. These two reasons explain the many effective nucleation positions and the increased fraction of intragranular AF and PF.

The precipitates act as nucleation sites for intragranular ferrite stemming from the low interface energy of heterogeneous nucleation. The number density, category, and size of the precipitates alter its capacity for ferrite nucleation and, hence, affect the formation of intragranular nucleated ferrite. Ti(C,N) was not an effective nucleation site, whereas V(C,N) had a small lattice mismatch with ferrite, which promoted ferrite nucleation, as confirmed by previous studies [31]. The submicron-scale complex precipitates, (Ti,V)(C,N) and (V,Ti)(C,N), with Ti(C,N) inside and V(C,N) on the surface, can form a certain orientation relationship with ferrite: $(001)_{precipitate}//(001)_{ferrite}$, $(100)_{precipitate}//(110)_{ferrite}$ [32]. Zhang et al. observed the orientation relationship (001) α // (110) V(C,N) using HRTEM [30]. Moreover, precipitates between 0.25-0.8 μm support ferrite nucleation very well [33,34]. The precipitate size positively correlates with ferrite nucleation capacity. An increased precipitate size enhances the ferrite nucleation capacity and facilitates intragranular ferrite transformations due to the gradual degradation of the nucleation energy barrier [2,35]. In addition, large precipitates possibly nucleated around abundant ferrite due to its external surface area, and the nucleation of intragranular AF or PF occurred at the inclusion surfaces.

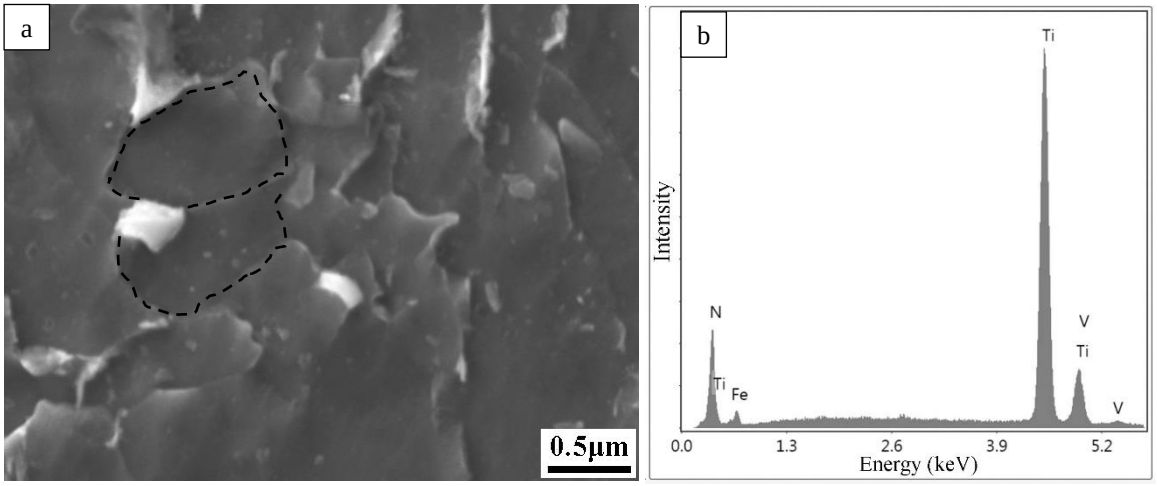


Figure 12. The morphology of intragranular nucleated ferrite (**a**) and the chemical composition of the precipitate (**b**).

The type of ferrite changed from LBF and GBF to AF and PF with increasing heat inputs. As well as heterogeneous nucleation induced by intragranular precipitates, the microstructural evolution also relates to the degree of supercooling. Dilatation curves were applied to understand the phase transformation kinetics of simulated CGHAZ with different heat inputs, as shown in Figure 13. The starting temperature of the ferrite transformation increased from 593 °C to 739 °C as the heat input increased from 25 to 75 kJ/cm, which indicated the decreased degree of supercooling.

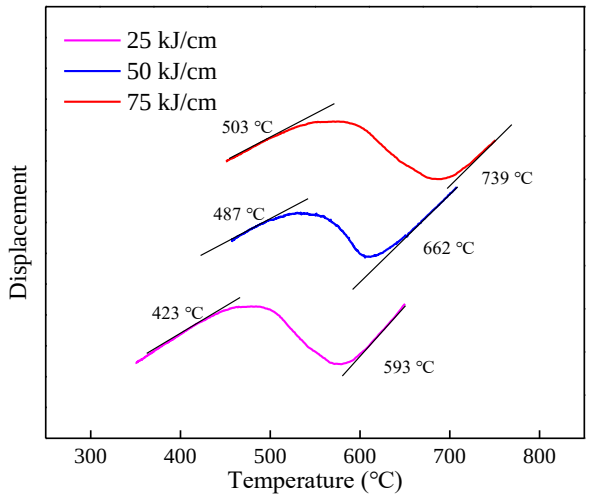


Figure 13. Dilatation curves and the Ar_3 points for the simulated samples with different heat inputs.

The variation of supercooling led to changes in the ferrite nucleation mode. The preferential nucleation sites changed from intergranular nucleation to intragranular nucleation with a decreased degree of supercooling. For the 25-kJ/cm sample, the diffusion of carbon was inhibited because of the high supercooling degree. LBF and GBF nucleated on the austenite grain boundaries and grew rapidly along a certain orientation. As a non-diffusive transformation, AF transformation occurred more commonly with a lower degree of supercooling, due to AF nucleation on the intragranular precipitate. For the 75-kJ/cm sample, carbon atoms readily diffused due to the low supercooling degree. PF nucleation occurred mainly on large precipitates and growth was independent of the PF boundary orientation.

Prior austenite grains (PAGs) were observed to estimate microstructural characteristics further (Figure 14). The mean PAG sizes increased from 45.5 to 53.8 μm as the heat input increased from 25 to 75 kJ/cm. The coarsening of PAG generally occurs with increasing heat

inputs. For the low-carbon Mo-V-Ti-N-B steel with different heat inputs, the insignificant PAG size increase was due to the pinning effect of 10–80-nm precipitates dispersed on the PAG boundaries.

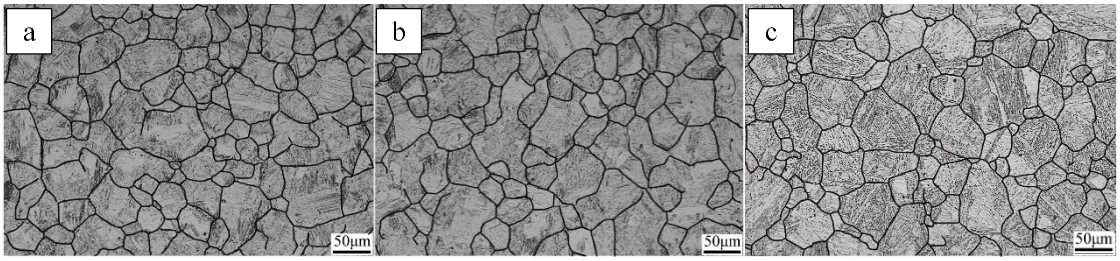


Figure 14. The morphology of PAGs of the simulated samples with heat inputs of 25 kJ/cm (**a**), 50 kJ/cm (**b**), and 75 kJ/cm (**c**).

The decrease in the MED and increase in the $f_{MTA} > 15°$ was mainly due to the amount of intragranular ferrite. The average coarse precipitate size, with V(C,N) enrichment on the surface, reached the critical nucleation size and promoted nucleation of intragranular ferrite with increasing heat inputs. Moreover, the large austenite grains, with wide intragranular and limited grain boundary spaces, promoted transformation of intragranular ferrite and restrained GBF transformation.

4.2. Effects of Different Heat Inputs on the CGHAZ Mechanical Properties

The secondary cracks perpendicular to the fracture surface of the simulated CGHAZ samples helped elucidate the fracture behavior. The hardness difference between the M/A constituent and the surrounding ferrite matrix usually resulted in a local stress concentration [20]. Therefore, the M/A constituent acted as a microcrack indicator that deteriorates the impact property [36]. The M/A constituents with high hardness initiate cleavage microcracks in all samples, and as shown in Figure 15, indicates that the crack passes straight through the GBF matrix and M/A constituents without any sample hindrances at 25 kJ/cm. The crack was deflected by the PAG boundary and arrested inside the PAG. Moreover, Figure 15b shows that the crack propagation path was also impeded by intragranular AF at 50 kJ/cm. However, the crack propagation paths of the sample at 75 kJ/cm were deflected at the grain boundaries of AF and PF (Figure 15c). The unit crack propagation path decreased from 18 to 4 μm as the heat input increased from 25 to 75 kJ/cm.

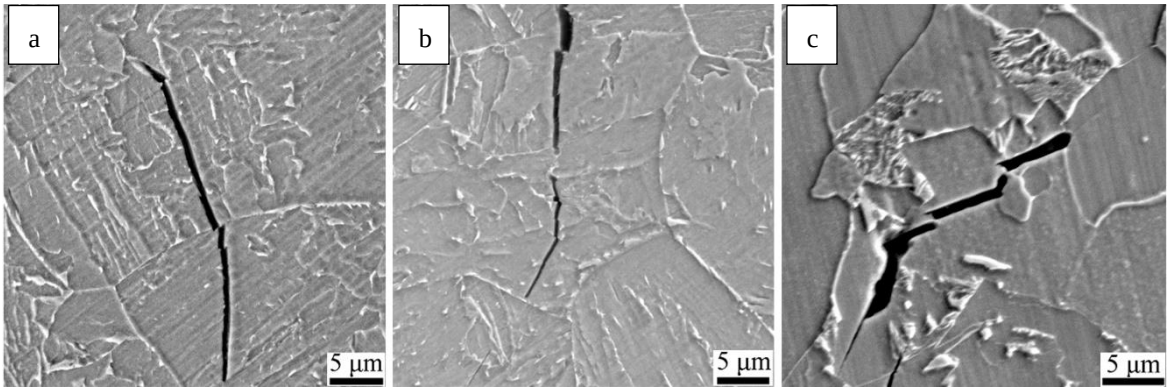


Figure 15. The crack propagation pathways of simulated samples with the heat inputs of 25 kJ/cm (**a**), 50 kJ/cm (**b**), and 75 kJ/cm (**c**).

To investigate the influence of the grain boundary on crack propagation, the band contrast map with the grain boundaries was examined. MTAs between 2–15° and >15° are represented by the red and green lines, respectively. Figure 16 shows that the crack propagation was continuous and uninterrupted through the low-angle grain boundaries

(grains 1–2, grains 2–3, grains 6–7, and grains 7–8), whereas the crack propagation deviated and even stopped at the high-angle grain boundaries (grains 3–4, grains 5–6, and grains 8–9), which indicated that the grain boundaries of AF and PF with an MTA higher than 15° impeded crack propagation. As a barrier to crack propagation, the high-angle grain boundary forces the crack to change its propagation direction to adapt to the new local grain orientation [37,38]. Moreover, the AF also hinders crack propagation and forms a small plastic deformation zone around the crack propagation path due to the high deformation ability of AF [25,39].

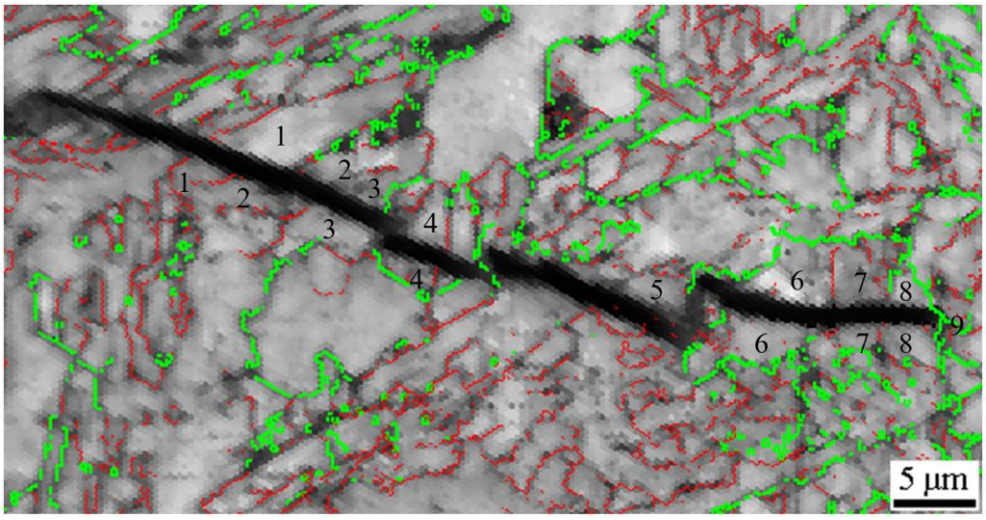


Figure 16. Band contrast map of crack propagation in simulated samples with a heat input of 50 kJ/cm.

The mixed microstructure changed from LBF and GBF to AF and PF as the heat input increased from 25 to 75 kJ/cm (Figure 3e). Combined with the EBSD analysis results shown in Figure 6, the microstructure variation led to an increase in the relative frequency of high-angle grain boundaries. With increased heat inputs, the hindering of crack propagation significantly improved due to the increased high-angle grain boundaries. It was difficult for cracks to propagate after initiation, which led to increased impact energy.

5. Conclusions

In this paper, the microstructures and impact properties of simulated CGHAZ in low-carbon Mo-V-Ti-N-B steel with different heat inputs were studied. The main conclusions are summarized as follows:

(1) The CGHAZ microstructure changed from LBF + GBF + M/A to AF + PF + M/A with increasing heat inputs from 25 to 75 kJ/cm. Moreover, the MED of the ferrite grains decreased from 7.6 μm to 4.2 μm, and the boundary fractions at MTAs higher than 15° increased from 20.3% to 45.5%;

(2) The degree of V(C,N) enrichment on the precipitate surface and the average size of coarse precipitates increased with increasing heat inputs, which provided the necessary thermal conditions and reached the critical size for intragranular ferrite nucleation. Increasing heat inputs also resulted in elevated Ar_3, which led to decreased LBF as well as increased AF and PF;

(3) Increasing the heat input from 25 to 75 kJ/cm led to significantly improved CGHAZ impact properties due to additional high-angle grain boundaries, which effectively impeded microcrack propagation.

Author Contributions: Q.W. (Qingfeng Wang) and M.Q. conceived and designed the experiments; H.F., Q.W (Qiuming Wang) and L.W. performed the experiments and processed the experimental

data; G.S. contributed to the analysis of the data and spell-checks words; M.Q. wrote the original draft; R.L. provided the test equipment and software and direct thermodynamic calculation. All authors have read and agreed to the published version of the manuscript.

Funding: This work was supported by the National Natural Science Foundation of China (Grant no. 51671165).

Institutional Review Board Statement: Not applicable.

Informed Consent Statement: Not applicable.

Data Availability Statement: Not applicable.

Conflicts of Interest: The authors declare that they have no known competing financial interests or personal relationships that could have appeared to influence the work reported in this paper.

References

1. Porter, L.F.; Repas, P.E. The Evolution of HSLA Steels. *JOM* **1982**, *34*, 14–21. [CrossRef]
2. Ricks, R.A.; Howell, P.R.; Barritte, G.S. The Nature of Acicular Ferrite in HSLA Steel Weld Metals. *J. Mater. Sci.* **1982**, *17*, 732–740. [CrossRef]
3. Kong, J.; Zhen, L.; Guo, B.; Li, P.; Wang, A.; Xie, C. Influence of Mo Content on Microstructure and Mechanical Properties of High Strength Pipeline Steel. *Mater. Des.* **2004**, *25*, 723–728. [CrossRef]
4. Kim, Y.M.; Lee, H.; Kim, N.J. Transformation Behavior and Microstructural Characteristics of Acicular Ferrite in Linepipe Steels. *Mater. Sci. Eng. A* **2008**, *478*, 361–370. [CrossRef]
5. Tomków, J.; Rogalski, G.; Fydrych, D.; Łabanowski, J. Advantages of the Application of the Temper Bead Welding Technique During Wet Welding. *Materials* **2019**, *12*, 915. [CrossRef] [PubMed]
6. Tomków, J.; Świerczyńska, A.; Landowski, M.; Wolski, A.; Rogalski, G. Bead-on-Plate Underwater Wet Welding on S700MC Steel. *Adv. Sci. Technol. Res. J.* **2021**, *15*, 288–296. [CrossRef]
7. Wang, G.; Yin, L.; Yao, Z.; Wang, J.; Jiang, S.; Zhang, Z.; Zuo, C. The Evolution and Distribution of Microstructures in High-Energy Laser-Welded X100 Pipeline Steel. *Materials* **2019**, *12*, 1762. [CrossRef]
8. Sauraw, A.; Sharma, A.K.; Fydrych, D.; Sirohi, S.; Gupta, A.; Świerczyńska, A.; Pandey, C.; Rogalski, G. Study on Microstructural Characterization, Mechanical Properties and Residual Stress of GTAW Dissimilar Joints of P91 and P22 Steels. *Materials* **2021**, *14*, 6591. [CrossRef] [PubMed]
9. Shanmugam, S.; Ramisetti, N.K.; Misra, R.; Hartmann, J.; Jansto, S.G. Microstructure and High Strength–Toughness Combination of a New 700MPa Nb-Microalloyed Pipeline Steel. *Mater. Sci. Eng. A* **2008**, *478*, 26–37. [CrossRef]
10. Guo, A.; Misra, R.; Liu, J.; Ling, C.; He, X.; Jansto, S.J. An Analysis of the Microstructure of the Heat-Affected Zone of an Ultra-Low Carbon and Niobium-Bearing Acicular Ferrite Steel Using EBSD and Its Relationship to Mechanical Properties. *Mater. Sci. Eng. A* **2010**, *527*, 6440–6448. [CrossRef]
11. Hu, J.; Du, L.X.; Wang, J.J.; Gao, C.R. Effect of Welding Heat Input on Microstructures and Toughness in Simulated CGHAZ of V–N High Strength Steel. *Mater. Sci. Eng. A* **2013**, *577*, 161–168. [CrossRef]
12. Wang, G.; Wang, J.; Yin, L.; Hu, H.; Yao, Z. Quantitative Correlation between Thermal Cycling and the Microstructures of X100 Pipeline Steel Laser-Welded Joints. *Materials* **2020**, *13*, 121. [CrossRef]
13. Esterling, K.E. *Introduction to the Physical Metallurgy of Welding*; Butterworths: London, UK, 1983.
14. Moeinifar, S. Influence of Thermal Simulated and Real Tandem Submerged Arc Welding Process on the Microstructure and Mechanical Properties of the Coarse Grained Heat Affected Zone. *Appl. Mech. Mater.* **2012**, *110–116*, 3191–3198. [CrossRef]
15. Dilawari, A.H.; Szekely, J.; Eagar, T.W. Electromagnetically and Thermally Driven Flow Phenomena in Electroslag Welding. *Metall. Trans. B* **1978**, *9*, 371–381. [CrossRef]
16. Debroy, T.; Szekely, J.; Eagar, T.W. Heat Generation Patterns and Temperature Profiles in Electroslag Welding. *Metall. Trans. B* **1980**, *11*, 593–605. [CrossRef]
17. Li, C.; Wang, Y.; Tao, H.; Han, B.; Li, L. Microstructure and Toughness of Coarse Grain Heat-Affected Zone of Domestic X70 Pipeline Steel during in-Service Welding. *J. Mater. Sci.* **2011**, *46*, 727–733. [CrossRef]
18. Lan, L.; Qiu, C.; Song, H.; Zhao, D. Correlation of Martensite–Austenite Constituent and Cleavage Crack Initiation in Welding Heat Affected Zone of Low Carbon Bainitic Steel. *Mater. Lett.* **2014**, *125*, 86–88. [CrossRef]
19. Lan, L.; Qiu, C.; Zhao, D.; Gao, X.; Du, L. Microstructural Characteristics and Toughness of the Simulated Coarse Grained Heat Affected Zone of High Strength Low Carbon Bainitic Steel. *Mater. Sci. Eng. A* **2011**, *529*, 192–200. [CrossRef]
20. Davis, C.L.; King, J.E. Cleavage Initiation in the Intercritically Reheated Coarse-Grained Heat-Affected Zone: Part I. Fractographic Evidence. *Metall. Mater. Trans. A* **1994**, *25*, 563–573. [CrossRef]
21. Matsuda, F.; Ikeuchi, K.; Fukada, Y.; Horii, Y.; Okada, H.; Shiwaku, T.; Shiga, C.; Suzuki, S. Review of Mechanical and Metallurgical Investigations of M-A Constituent in Welded Joint in Japan. *Trans. JWRI* **1995**, *24*, 1–24.

22. Chen, J.H.; Kikuta, Y.; Araki, T.; Yoneda, M.; Matsuda, Y. Micro-Fracture Behaviour Induced by M-A Constituent (Island Martensite) in Simulated Welding Heat Affected Zone of HT80 High Strength Low Alloyed Steel. *Acta Metall.* **1984**, *32*, 1779–1788. [CrossRef]
23. Wang, X.L.; Wang, Z.Q.; Dong, L.L.; Shang, C.J.; Ma, X.P.; Subramanian, S.V. New Insights into the Mechanism of Cooling Rate on the Impact Toughness of Coarse Grained Heat Affected Zone from the Aspect of Variant Selection. *Mater. Sci. Eng. A* **2017**, *704*, 448–458. [CrossRef]
24. Zhang, Y.; Shi, G.; Sun, R.; Guo, K.; Wang, Q. Effect of Si Content on the Microstructures and the Impact Properties in the Coarse-Grained Heat-Affected Zone (CGHAZ) of Typical Weathering Steel. *Mater. Sci. Eng. A* **2019**, *762*, 138082. [CrossRef]
25. Xiong, Z.; Liu, S.; Wang, X.; Shang, C.; Li, X.; Misra, R. The Contribution of Intragranular Acicular Ferrite Microstructural Constituent on Impact Toughness and Impeding Crack Initiation and Propagation in the Heat-Affected Zone (HAZ) of Low-Carbon Steels. *Mater. Sci. Eng. A* **2015**, *636*, 117–123. [CrossRef]
26. Shi, G.; Zhao, H.; Zhang, S.; Wang, Q.; Zhang, F. Microstructural Characteristics and Impact Fracture Behaviors of Low-Carbon Vanadium-Microalloyed Steel with Different Nitrogen Contents. *Mater. Sci. Eng.* **2020**, *769*, 138501.1–138501.13. [CrossRef]
27. Shi, G.; Luo, B.; Zhang, S.; Wang, Q.; Zhao, H. Microstructural Evolution and Mechanical Properties of a Low-Carbon V–N–Ti Steel Processed with Varied Isothermal Temperatures. *Mater. Sci. Eng. A* **2021**, *801*, 140396. [CrossRef]
28. Shi, Z.; Yang, C.; Wang, R.; Hang, S.; Feng, C.; Chu, J.; Wang, Q. Effect of Nitrogen on the Microstructures and Mechanical Properties in Simulated CGHAZ of Vanadium Microalloyed Steel Varied with Different Heat Inputs. *Mater. Sci. Eng. A* **2016**, *649*, 270–281. [CrossRef]
29. Shi, Z.; Wang, R.; Hang, S.; Feng, C.; Wang, Q.; Yang, C. Effect of Nitrogen Content on the Second Phase Particles in V–Ti Microalloyed Shipbuilding Steel during Weld Thermal Cycling. *Mater. Des.* **2016**, *96*, 241–250. [CrossRef]
30. Zhang, J.; Xin, W.; Luo, G.; Wang, R.; Meng, Q.; Xian, S. Effect of Welding Heat Input on Microstructural Evolution, Precipitation Behavior and Resultant Properties of the Simulated CGHAZ in High-N V-Alloyed Steel. *Mater. Charact.* **2020**, *162*, 110201. [CrossRef]
31. Gregg, J.M.; Bhadeshia, H. Solid-State Nucleation of Acicular Ferrite on Minerals Added to Molten Steel. *Acta Mater.* **1997**, *45*, 739–748. [CrossRef]
32. Miyamoto, G.; Shinyoshi, T.; Yamaguchi, J.; Furuhara, T.; Maki, T.; Uemori, R. Crystallography of Intragranular Ferrite Formed on (MnS + V(C, N)) Complex Precipitate in Austenite. *Scr. Mater.* **2003**, *48*, 371–377. [CrossRef]
33. Lee, J.-L. Evaluation of the Nucleation Potential of Intragranular Acicular Ferrite in Steel Weldments. *Acta Metall. Mater.* **1994**, *42*, 3291–3298. [CrossRef]
34. Fan, H.; Shi, G.; Peng, T.; Wang, Q.; Wang, L.; Wang, Q.; Zhang, F. N-Induced Microstructure Refinement and Toughness Improvement in the Coarse Grain Heat-Affected Zone of a Low Carbon Mo–V–Ti–B Steel Subjected to a High Heat Input Welding Thermal Cycle. *Mater. Sci. Eng. A* **2021**, *824*, 141799. [CrossRef]
35. Shi, Z.; Chai, X.; Chai, F.; Su, H.; Pan, T.; Wang, Q.; Wang, R.; Yang, C. The Mechanism of Intragranular Ferrite Formed on Ti-Rich (Ti,V)(C,N) Precipitates in the Coarse Heat Affected Zone of a V–N–Ti Microalloyed Steel. *Mater. Lett.* **2016**, *175*, 266–270. [CrossRef]
36. Lan, L.; Qiu, C.; Zhao, D.; Gao, X.; Du, L. Analysis of Martensite–Austenite Constituent and Its Effect on Toughness in Submerged Arc Welded Joint of Low Carbon Bainitic Steel. *J. Mater. Sci.* **2012**, *47*, 4732–4742. [CrossRef]
37. Diáz-Fuentes, M.; Iza-Mendia, A.; Gutiérrez, I. Analysis of Different Acicular Ferrite Microstructures in Low-Carbon Steels by Electron Backscattered Diffraction. Study of Their Toughness Behavior. *Metall. Mater. Trans. A* **2003**, *34*, 2505–2516. [CrossRef]
38. Zhong, Y.; Xiao, F.; Zhang, J.; Shan, Y.; Wei, W.; Yang, K. In Situ TEM Study of the Effect of M/A Films at Grain Boundaries on Crack Propagation in an Ultra-Fine Acicular Ferrite Pipeline Steel. *Acta Mater.* **2006**, *54*, 435–443. [CrossRef]
39. Cui, H.B.; Xie, G.M.; Luo, Z.A.; Ma, J.; Misra, R. The Microstructural Evolution and Impact Toughness of Nugget Zone in Friction Stir Welded X100 Pipeline Steel. *J. Alloys Compd.* **2016**, *681*, 426–433. [CrossRef]